Fracture mechanics of delamination defects in multilayer dielectric coatings

H. P. H. Liddell,[1,2,*] K. Mehrotra,[1,3] J. C. Lambropoulos,[1,2,3] and S. D. Jacobs[1,2]

[1]Laboratory for Laser Energetics, University of Rochester, 250 East River Road, Rochester, New York 14623, USA

[2]Program of Materials Science, University of Rochester, Rochester, New York 14627, USA

[3]Department of Mechanical Engineering, University of Rochester, Rochester, New York 14627, USA

*Corresponding author: hhow@lle.rochester.edu

Received 17 July 2013; revised 8 October 2013; accepted 11 October 2013;
posted 14 October 2013 (Doc. ID 194085); published 4 November 2013

During the fabrication of multilayer-dielectric (MLD) thin-film-coated optics, such as the diffraction gratings used in OMEGA EP's pulse compressors, acid piranha cleaning can lead to the formation of chemically induced delamination defects. We investigate the causes of these defects and describe a mechanism for the deformation and failure of the MLD coating in response to hydrogen peroxide in the cleaning solution. A fracture mechanics model is developed and used to calculate the crack path that maximizes the energy-release rate, which is found to be consistent with the characteristic fracture pattern observed in MLD coating delamination defects. © 2013 Optical Society of America

OCIS codes: (310.6845) Thin film devices and applications; (230.4170) Multilayers; (310.4925) Other properties (stress, chemical, etc.).

http://dx.doi.org/10.1364/AO.52.007689

1. Introduction

Multilayer-dielectric (MLD) thin-film coatings are widely used to produce high-quality optical components, having diverse applications ranging from Bragg mirrors to polarizer optics. Hafnia (HfO_2) and silica (SiO_2) multilayers are frequently used to fabricate MLD diffraction gratings for high-intensity laser systems because of the inherently high laser-damage resistance of this material combination [1,2]. The laser-damage thresholds of MLD gratings are typically well below those of the constituent dielectric materials themselves, however, because surface texture, contamination, and microscopic defects can dramatically affect laser-damage resistance [3–9].

MLD coatings are susceptible to a variety of unique defects and phenomena arising from fabrication and storage, including nodules [5,6], pits [4,7], absorption of volatilized contaminants from vacuum [10], and optical instabilities resulting from moisture penetration into porous oxide layers from humid air [11,12]. Patterned optical components such as MLD diffraction gratings require aggressive cleaning operations to remove photoresist and other lithographic residues. Unfortunately, some of the most-effective cleaning methods—usually involving high temperatures and strong acids or bases—can themselves induce chemical degradation and thermal stresses in the coating, leading to delamination and defects [9,13].

Micron-scale delamination defects have been observed on MLD coatings after exposure to hot acid piranha solution—a mixture of hydrogen peroxide and sulfuric acid that is commonly used to clean MLD gratings [9,14–16]. Delamination defects are distinguished by a characteristic pattern of crescent-shaped fractures in the coating, with the layers uplifted at the defect site. Because these features interrupt the continuity of the MLD surface, they may cause electric-field enhancement and reduced

1559-128X/13/327689-10$15.00/0

laser-damage thresholds. While we have been able to largely avoid the production of cleaning defects by reducing piranha solution temperatures to 40°C [9], a thorough understanding of the causes and formation mechanism of delamination defects will be important in the continued development of cleaning technologies.

In the proposed defect mechanism, the deformation and fracture of the coating are explained by assuming a localized pressure buildup in a small volume of acid piranha trapped in the coating. The associated fracture mechanics problem is that of a pressure-loaded blister in a multilayer material—an extension of the pressurized circular blister treated by Jensen [17]. The appropriate length scale for the multilayer blister problem is explored. Finally, the predicted path of a crack propagating through the MLD coating layers is compared with the observed cross-sectional geometry of a defect.

2. Materials and Methodology

The MLD samples used in this study were 3 mm thick, 100 mm diameter BK7 substrates coated by electron-beam evaporation in a high reflector design (a modified quarter-wave stack of high- and low-index layers) with an extra-thick top layer [18]. The coating comprised 28 layers of alternating HfO_2 and SiO_2 with a bottom layer of HfO_2 and top layer of SiO_2. The total coating thickness was 5.0 μm, with typical layer thicknesses of 190 nm for the silica layers and 142 nm for the hafnia layers. Samples were not patterned or etched. For cleaning experiments, each sample was broken into eight wedges.

Defects were generated by submerging the samples in an acid piranha solution. For each test, 400 mL of acid piranha solution were prepared and cooled to room temperature. The ratio of sulfuric acid to hydrogen peroxide was either two parts H_2SO_4 to one part H_2O_2 (2:1 piranha) or five parts H_2SO_4 to one part H_2O_2 (5:1 piranha), depending on the test. After preparation, the piranha solution was used within 24 h to limit degradation. Except as noted, samples were submerged into the piranha solution at room temperature, heated to the prescribed soak temperature over a ramp period of 30 min, held at the soak temperature for the specified duration, and then cooled to room temperature over 30 min using an ice bath. After the MLD samples were removed from the solution, they were rinsed with deionized water and dried using a filtered nitrogen gun [19]. Samples were inspected in a Leica Nomarski microscope after the piranha treatment and evaluated for defect formation.

3. Characterization of the Delamination Defect

A. Microscopy

Nomarski micrographs of representative delamination defects are shown in Fig. 1. The piranha treatments for the samples shown are specified in the captions. Delamination defects had typical dimensions of 20–50 μm and featured a characteristic array of circular- and crescent-shaped cracks radiating out from an initiating point, typically an existing surface feature. Some defects were associated with nodules, as shown in Figs. 1(a) and 1(b), while other defects were paired with pieces of debris, as in Fig. 1(c), or formed in groups along scratches, as in Figs. 1(d) and 1(e). Occasionally, delamination defects were identified that seemed not to be linked to any other artifact, as shown in Fig. 1(f). Because we have only rarely observed defects in this final category, they may be connected with small features that simply could not be resolved in the light microscope. Defects sometimes involved many coating layers, as in Figs. 1(a) and 1(c), or just a few coating layers, as in Fig. 1(b).

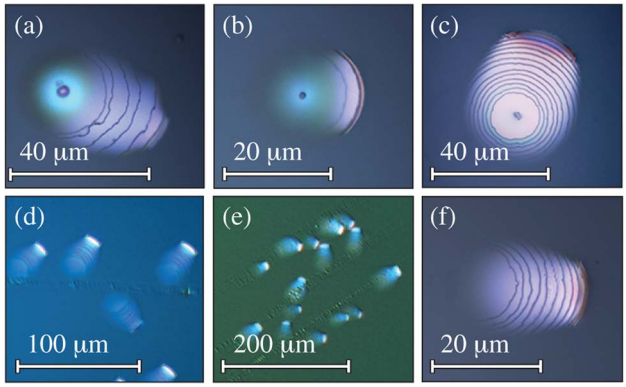

Fig. 1. Nomarski micrographs of representative delamination defects. (a) and (b) Defects associated with nodules. (c) A defect associated with a piece of surface debris. (d) and (e) Defects that formed along scratches. (f) A defect that was not observed with any apparent surface feature. Defects were generated by submerging the samples in 2:1 piranha, with the following temperature treatments: (a) and (b) 90°C soak for 2 h with 30 min heating and cooling ramps; (c) sample submerged at 70°C and cooled to room temperature over 2 h; (d) and (e) sample submerged at 90°C and cooled over 30 min; and (f) sample submerged at 70°C and cooled over 30 min.

Because the oxide layers of the coating are transparent to white light, cracks in each layer are visible in the optical micrographs of Fig. 1. The approximate depths of cracks in the multilayer were determined by recording the z position of best focus, and in all cases the crack nearest to the "initiating" artifact was located in the deepest coating layer involved in the defect. The crack front farthest from this central artifact was at the surface layer, suggesting that delamination defects nucleate within the coating, not at the surface.

Defects were examined in a scanning electron microscope (SEM) to further probe their geometries. Because the SEM reveals only the sample's surface, a top-down SEM image [Fig. 2(a)] revealed only the arc-shaped crack in the uppermost coating layer. To examine the defect's cross section, focused-ion-beam (FIB) milling was used to cut a trench in the MLD coating, bisecting a delamination defect. A thin layer of platinum was locally deposited immediately

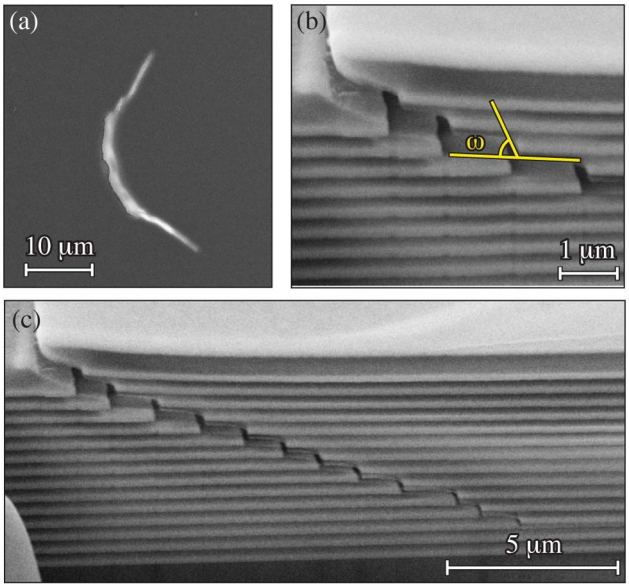

Fig. 2. Scanning electron microscope (SEM) images showing (a) a delamination defect observed from a bird's eye view, showing its surface structure; (b) a high-magnification, cross-sectional view of a defect bisected by focused-ion-beam (FIB) milling, showing the crack path through MLD layers near the surface. The angle ω shows how the crack kink angles were measured for the fracture mechanics analysis; and (c) a larger view of the FIB-milled defect's cross section.

prior to milling to enable the beam to cut a clean cross section instead of gradually eroding the multilayer. The resulting cross-sectional views, shown in Figs. 2(b) and 2(c), reveal a zigzagging crack in the upper 24 layers of the coating (the bottom two layer pairs were apparently unaffected in this particular case). The uplifting of the coating at the defect site and the separation between crack faces explains the bright appearance of delamination defects in the optical microscope images of Fig. 1. The uplifting of the coating also explains previous nanoindentation results showing that delamination defects are more compliant than the surrounding coating [20]. The kink angle ω shown in Fig. 2(b) illustrates how these angles were measured for the fracture mechanics analysis of Section 5.

B. Causes of Delamination Defects

A screening experiment was carried out to investigate the factors contributing to defect formation during piranha cleaning. The experiment was designed using JMP statistical software and design-of-experiments (DOE) methodology to randomize trial order and to choose appropriate factor levels. The effects of five parameters were studied: (1) the age of the MLD coating at the time of cleaning (because the intrinsic coating stress level has been shown to vary with time [21–24]); (2) the ratio of sulfuric acid to hydrogen peroxide (piranha ratio) in the acid piranha solution; (3) the solution temperature during the soak period; (4) the soak duration, not including time spent ramping up to the soak temperature or cooling to room temperature; and (5) whether or not the sample was heat shocked by submerging it directly into hot piranha at the soak temperature (rather than slowly heated to the soak temperature over 30 min). The effect of rapid heating was of interest because evaporated MLD coatings are susceptible to tensile stress fracture [21,22]. Hafnia and silica thin films have lower coefficients of thermal expansion than does the BK7 substrate, leading to the development of tensile-coating stresses as the optic is heated [13]. Defect density on the MLD sample after cleaning (number of delamination defects per unit surface area) was used as the response for the experiment. Analysis-of-variances (ANOVA) results from the experiment are presented in Table 1.

Assigning a confidence limit of 95%, the piranha ratio was the only factor judged statistically significant in this experiment (denoted by asterisks in Table 1). The samples treated with 2:1 piranha had defect densities that were, on average, an order-of-magnitude higher than the samples cleaned with 5:1 piranha, indicating that hydrogen peroxide plays an important role in cleaning-induced defect

Table 1. ANOVA Results for the Delamination Defect Screening Experiment

Factor	Level	Mean Defect Density (defects/cm^2)	Sum of Squares	Mean Square	Degrees of Freedom	F Ratio	Prob > F (p Value)
Coating age	2 weeks	1.92	9.57	4.78	2	0.96	0.39
	6 weeks	1.47					
	12 weeks	0.95					
Piranha ratio (H_2SO_4:H_2O_2)	5:1	0.24	68.57	68.57	1	13.74	0.001***
	2:1	2.76					
Soak temperature	50°C	1.18	2.09	1.05	2	0.21	0.81
	70°C	1.44					
	90°C	1.69					
Soak time	0 min	0.98	13.31	6.66	2	1.33	0.28
	30 min	1.23					
	60 min	2.12					
Heat shock	Shocked	1.06	7.56	7.56	1	1.52	0.23
	Not shocked	1.82					
Error estimate	—	—	154.59	4.99	31	—	—

***Significance at the $p \leq 0.001$ level.

formation. Anecdotally, this result is supported by the fact that we have regularly observed delamination defects on MLD samples exposed to acid piranha (and on samples exposed to 30% hydrogen peroxide) but never on samples exposed to non-peroxide-containing chemicals that we have tested, including sulfuric acid and a variety of solvents and commercial photoresist strippers. Trends in the data that warrant further investigation also suggest connections between increased defect formation and high piranha temperatures, long soak duration, and freshly deposited MLD coatings.

C. Process of Defect Formation

Typically, delamination defects are observed immediately after piranha cleaning: by the time a sample can be rinsed, dried, and transferred to the microscope, all cleaning-induced defects have already formed. In one experiment, however, the real-time formation of delamination defects was witnessed firsthand during a routine inspection of an MLD sample approximately 45 min after removal from the piranha solution.

Frames captured from a video of defect formation, showing a 75 μm × 75 μm area as viewed in Nomarski, are shown in Fig. 3 (Media 1). The formation process took about 20 s. The defect grew with a round shape at first, shown in Figs. 3(a)–3(c), then expanded to an oblong shape as it broke through the layers of the MLD [Figs. 3(d) and 3(e)]. The defect had nearly reached its final size about 3 s after it began to form and reached a stable geometry [Fig. 3(h)] after about 20 s. The bright spot in the lower part of Figs. 3(a)–3(d) is another smaller artifact. At the 3-s mark [Fig. 3(e)], the newly formed defect merged with this small artifact.

Figure 4 shows the evolution of a 160 μm × 140 μm area surrounding the defect of Fig. 3. Two new defects formed in this region: one appearing in Fig. 4(b) and another in Fig. 4(c). The just-formed defects flickered distinctly and appeared to be liquid filled, with a pulsating effect possibly caused by

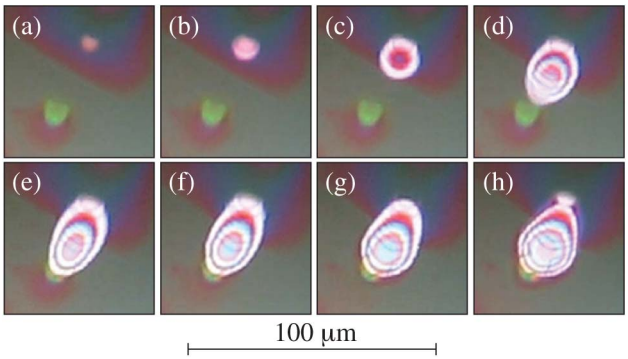

Fig. 3. Series of 75 μm × 75 μm frames captured from a Nomarski microscope video (Media 1) of an individual delamination defect's formation approximately 45 min after a 2 h submersion in 2:1 piranha at 90°C. The defect's development is shown (a) 0 s, (b) 2.0 s, (c) 2.6 s, (d) 2.7 s, (e) 3.0 s, (f) 6.0 s, (g) 11.0 s, and (h) 20.0 s after it began to form.

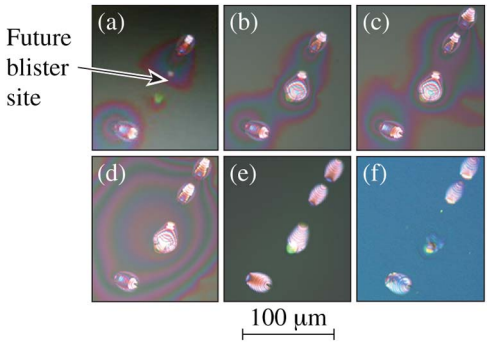

Fig. 4. Nomarski micrographs of a 160 μm × 140 μm region containing the defect seen in Fig. 3. Images were captured (a) 45 min, (b) 60 min, (c) 61 min, (d) 100 min, (e) 48 h, and (f) 6 months after the sample was removed from the piranha solution.

rapid evaporation. The defects were initially surrounded by regions of trapped fluid, which moved about and agglomerated into larger areas over time [see Figs. 4(a)–4(d)]. These features may be similar to the "moisture penetration patterns" described by Macleod and Richmond [11], involving the incorporation of fluid into the porous structure of oxide layers.

Several hours after piranha cleaning, the trapped liquid had escaped from the MLD coating, and the flickering had stopped. A difference in optical thickness remained, leading to the bright appearance of mature delamination defects in Nomarski microscopy [Fig. 4(e)]. Interestingly, when the MLD sample was reinspected several months later [Fig. 4(f)], the defect of Fig. 3 had nearly disappeared, possibly after collapsing into optical contact. The smaller, overlapping defect was still apparent.

4. Mechanism of Delamination Defect Formation

We propose a mechanism to explain the primary features of delamination defects presumed from experimental observations; namely, that (1) hydrogen peroxide is essential to defect formation; (2) delamination defects are typically associated with an existing flaw that interrupts the coating; (3) defects are initially filled with liquid; (4) the crack in the multilayer advances in a zigzagging fashion upward toward the surface; (5) separation of crack faces leads to a permanent uplifting of the coating and a change in optical thickness at the defect site; but (6) delamination defects can "heal" by collapsing into optical contact.

A proposed mechanism for defect formation that satisfies all of the above requirements is shown schematically in Fig. 5. First, acid piranha penetrates into the MLD coating [Fig. 5(a)] through a large pore, small scratch, or defect (not shown), and a small volume of piranha becomes trapped in the coating at an interface where adhesion has locally failed (between layers or between substrate and coating). Pressure builds up at this location because of the evolution of oxygen gas from hydrogen peroxide in the trapped piranha, and the MLD layers deform into a circular blister to accommodate the increasing pressure

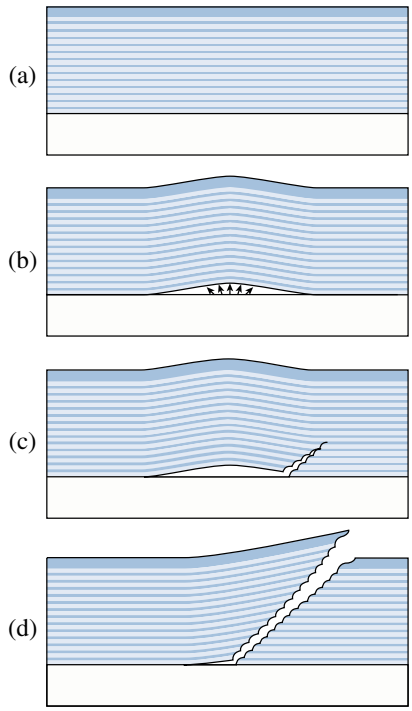

Fig. 5. Schematic illustrating the hypothesized delamination defect formation mechanism: (a) undisturbed MLD coating, (b) initial pressure development in coating and deformation, (c) kinked fracture at edge of pressurized blister, and finally (d) propagation of the crack to MLD surface. Light bands represent hafnia layers in the coating, while dark bands represent silica layers.

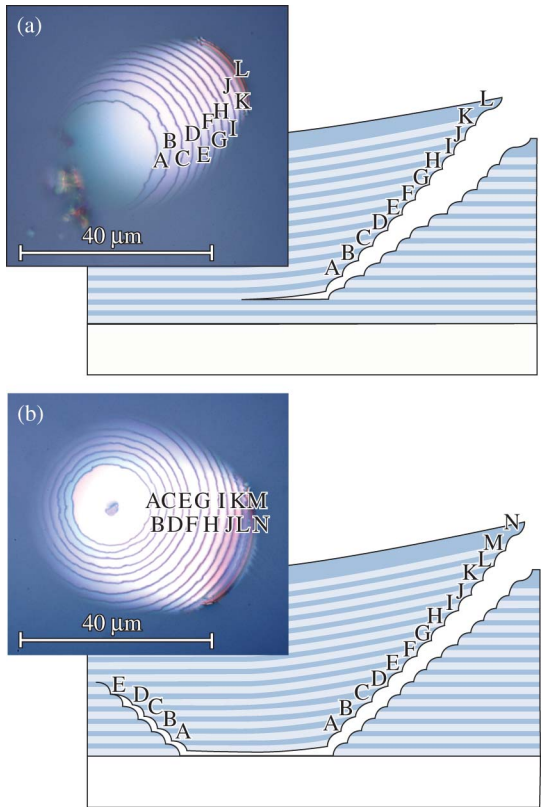

Fig. 6. Nomarski micrographs of two delamination defects with schematics showing hypothesized cross-sectional geometries. (a) Defect initiated between the second and third MLD layer pairs, with arc-shaped cracks. (b) Substrate-initiated defect with fracture through all 14 layer pairs. Fracture in the bottom few layers occurred as circular cracks at the blister's perimeter, while cracks in upper layers were arc-shaped.

[Fig. 5(b)]. Once the critical stress for fracture is reached in the deforming MLD, crack propagation occurs. The crack may initially propagate along the interface (increasing the debond area), but to explain the characteristic fracture pattern, the crack must eventually kink upward into the multilayer [Fig. 5(c)]. The crack propagates through the MLD coating to the surface, where accumulated oxygen gas escapes, relieving built-up pressure and collapsing the inflated blister structure. The final defect geometry includes a gap between crack faces [Fig. 5(d)], but if the layers later collapse into contact, eliminating air gaps, the defect may appear to have "healed."

Figure 6 shows hypothesized cross-sectional geometries of two observed delamination defects. Twelve arc-shaped cracks, labeled A–L, were counted in the Nomarski micrograph of defect (a). This defect likely initiated between layers 4 (silica) and 5 (hafnia), and each observed arc-shaped crack involved one hafnia/silica layer pair. In defect (b), 14 cracks (A–N) were identified, consistent with a substrate-initiated blister with fracture through all 28 layers. At least five of the 14 cracks (A–E) were circular. Cracks in the upper layer pairs (F–N) were arc shaped with successively shorter arc lengths. The hypothesized geometry in this case is similar to (a), but with complete circular cracks in the initial few layers with an asymmetrical geometry developing as the crack propagated upward.

The proposed mechanism requires that a small volume of liquid become trapped between layers of the MLD coating. The original entry path must not be a viable path for the escape of gas or liquid; otherwise, high pressures could not develop in the cavity because the oxygen gas evolved from the decomposition of acid piranha could simply travel out of the volume to relieve pressure. Considering the multilayer structure of the thin-film coating, we suggest the coefficient of thermal-expansion mismatch between hafnia and silica layers as an explanation: if the MLD layers deform or shift with respect to each other during elevated temperature cleaning, a path to the surface through adjacent layers could become blocked, and pressure could develop freely in a void containing trapped acid piranha.

5. Fracture Mechanics

A. Material Properties of Dielectric Layers and MLD Coatings

The properties of thin films can be sensitive to the deposition technique [25,26], and therefore it can be unwise to assume thin-film properties for one coating based on data from a different coating, unless it is known that the deposition method was the same.

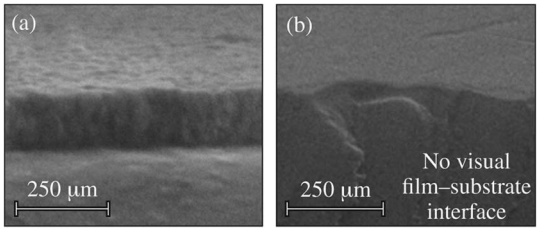

Fig. 7. SEM images showing cross sections of single-layer oxide films used in nanoindentation experiments. (a) A 160 nm layer of hafnia. (b) A 180 nm layer of silica. There was no visible interface between the substrate and the amorphous silica film.

Nanoindentation of single layer hafnia and silica films was carried out to accurately estimate the elastic moduli of the MLD layers. Cross sections of the films tested are shown in Fig. 7. The film thicknesses (135 nm for hafnia and 180 nm for silica) were similar to the thicknesses of those layers in the multilayer coating, and the deposition technique was the same as that used for the MLD coating layers. To avoid substrate effects in the nanoindentation measurements, mechanical properties were assessed using data from indenter penetration into only the top 10%–20% of the total film thickness. The average Young's moduli calculated for the single layer films were $E_{\mathrm{haf}} = 128 \pm 12.5$ GPa (average± standard deviation of four measurements) for hafnia and $E_{\mathrm{sil}} = 92 \pm 5$ GPa for silica. These measurements were within ~25% of moduli reported by Thielsch *et al.* [25] for thin-film hafnia (deposited by reactive evaporation) and silica (deposited by plasma ion-assisted deposition). Poisson ratio ν for the films was estimated from reported values [27,28], and shear and bulk moduli μ and B were calculated from E and ν using the relations $\mu = E/2(1+\nu)$ and $B = E/3(1-2\nu)$, respectively.

MLD coating properties were estimated from the single-layer film properties determined by nanoindentation experiments. Upper and lower limits on shear modulus and bulk modulus were calculated by the rule of mixtures:

$$\mu_{\mathrm{MLD}}^{\mathrm{upper}} = \mu_{\mathrm{haf}} V_{\mathrm{haf}} + \mu_{\mathrm{sil}} V_{\mathrm{sil}},$$
$$B_{\mathrm{MLD}}^{\mathrm{upper}} = B_{\mathrm{haf}} V_{\mathrm{haf}} + B_{\mathrm{sil}} V_{\mathrm{sil}}, \tag{1}$$

and

$$\frac{1}{\mu_{\mathrm{MLD}}^{\mathrm{lower}}} = \frac{V_{\mathrm{haf}}}{\mu_{\mathrm{haf}}} + \frac{V_{\mathrm{sil}}}{\mu_{\mathrm{sil}}}, \quad \frac{1}{B_{\mathrm{MLD}}^{\mathrm{lower}}} = \frac{V_{\mathrm{haf}}}{B_{\mathrm{haf}}} + \frac{V_{\mathrm{sil}}}{B_{\mathrm{sil}}}, \tag{2}$$

where V_{haf} and V_{sil} are the volume fractions of hafnia and silica ($V_{\mathrm{haf}} = 0.39$ and $V_{\mathrm{sil}} = 0.61$ for the MLD used in this work). The calculated lower and upper limits on bulk modulus were 58.4 and 63.4 GPa, respectively, and the limits on shear modulus were 44.5 and 45.2 GPa, respectively. These bounds were averaged to estimate the bulk and shear moduli for the multilayer. Poisson ratio and Young's modulus for the MLD were calculated from these moduli using the relations

$$\nu = \frac{3B - 2\mu}{6B + 2\mu}, \quad E = 2\mu(1+\nu). \tag{3}$$

Bulk properties for the BK7 substrate were from Schott product literature [29]. Material properties are summarized in Table 2.

B. Contributions of Pressure and Intrinsic Stress to Blister Deformation

In Section 4, it was hypothesized that the delamination defect is initiated by pressure developed in a small, disk-shaped volume of acid piranha trapped in the coating. We therefore modeled the blister (prior to fracture) as a circular plate of thickness h and radius R, subjected to an internal pressure p_c and an equibiaxial intrinsic stress σ, and fixed to a thick substrate at its edges ($r = R$, where r is the radial coordinate), as shown in Fig. 8. The residual stresses in an evaporated MLD coating can be significant, and the pressure p_c evolved from piranha decomposition might not be large, so the effects of both loadings are considered in this analysis. The normal displacements of the plate are given by $w(r)$.

Jensen [17] showed that, in nondimensional form, the von Kármán plate equations for the situation shown in Fig. 8 can be written as

$$\frac{1}{12(1-\nu^2)}\rho\frac{d}{d\rho}\left[\frac{1}{\rho}\frac{d}{d\rho}(\rho\xi)\right] - \bar{\varphi}\xi + \frac{p_c R^4}{2Eh^4}\rho^2 = \frac{\sigma R^2}{Eh^4}\xi,$$
$$\rho\frac{d}{d\rho}\left[\frac{1}{\rho}\frac{d}{d\rho}(\rho\bar{\varphi})\right] + \frac{1}{2}\xi^2 = 0,$$
$$\xi(\rho) = -\frac{d\bar{w}}{d\rho}, \quad \bar{\varphi}(\rho) = \frac{R\varphi}{Eh^3}, \quad \varphi = \frac{d\Phi}{dr}, \tag{4}$$

where ν and E are the Poisson ratio and Young's modulus of the thin-film coating, Φ is the Airy stress function, and ρ and $\bar{w}$ are nondimensional quantities defined by $\rho = r/R$ and $\bar{w} = w/h$. For plate behavior, the appropriate boundary conditions are zero slope at the center of the blister, no rotations or displacements at the fixed edges, and $\bar{w}$ bounded everywhere.

Because the normalized pressure $p_c R^4/Eh^4$ is small (typically in the range of 0.007–0.474, with a representative value of 0.06), the pressure is carried

Table 2. Material Properties Used in the Fracture Mechanics Analysis

Material	Young's Modulus E (GPa)	Poisson Ratio ν	Shear Modulus μ (GPa)	Bulk Modulus B (GPa)
BK7 (bulk)	82	0.21	33.9	47.1
SiO_2 (thin film)	95	0.17	40.6	48.0
HfO_2 (thin film)	130	0.25	52.0	86.7
MLD coating	108	0.20	44.7	60.6

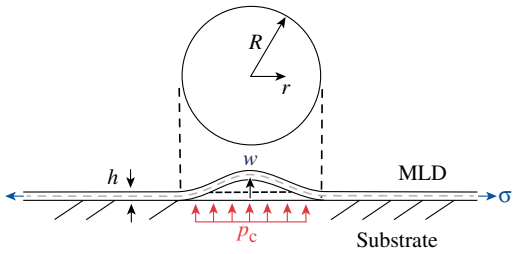

Fig. 8. Schematic of a pressurized blister in an MLD film with a residual film stress.

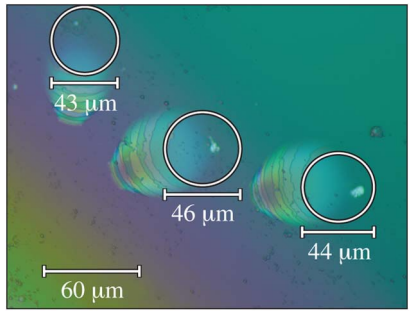

Fig. 9. Measurement of blister diameter.

by bending of the plate (rather than by membrane forces causing stretching). Therefore, bending is the dominant deformation mode, implying that the nonlinear $\overline{\varphi}\xi$ term in Eq. (4) can be neglected. The first equation can then be uncoupled from the second, and the resulting ordinary differential equation can be written as

$$\rho^2\xi'' + \rho\xi' - (S\rho + 1)\xi = -P\rho^3, \tag{5}$$

where prime indicates differentiation with respect to ρ. Two new nondimensional quantities, $S = 12(1-\nu^2)\sigma R^2/Eh^2$ (residual stress term) and $P = 6(1-\nu^2)p_c R^4/Eh^4$ (pressure term), were introduced for convenience. In the special case of negligible residual stresses, $S = 0$ and Eq. (5) reduces to an equidimensional Euler–Cauchy equation. Applying the boundary conditions, the solution for the $\sigma = 0$ case is

$$\xi(\rho) = -\frac{P}{8}(\rho^3 - \rho) \tag{6}$$

and

$$\bar{w}(\rho) = -\int \xi \mathrm{d}\rho = \frac{P}{32}(\rho^4 - 2\rho^2 + 1). \tag{7}$$

Returning to the general case [Eq. (5)], it can be shown that the solution for $\xi(\rho)$ can be given in terms of modified Bessel functions of the first and second kind and the Meijer G function. The solution $\xi(\rho)$ could not be readily integrated to find the blister deflections $\overline{w}(\rho)$ in closed form. An approximate solution was found by expanding all products in the expression for $\xi(\rho)$ and integrating term by term. The integrals of all but one term in the expanded form of $\xi(\rho)$ could be expressed in standard mathematical functions, and the remaining term was approximated by a five-term power series and integrated. The resulting approximation for $\overline{w}(\rho)$ agreed with the closed-form solution [Eq. (7)] for $\sigma \to 0$. A few specific cases are now considered.

Geometrical and material properties were selected as follows: $E = 108$ GPa and $\nu = 0.20$ (see Table 2), $h = 5$ μm (the thickness of the MLD coating), and $R = 20$ μm (estimated by measuring the diameter of the first fracture ring in micrographs of typical delamination defects, as shown in Fig. 9). It was difficult to accurately determine the residual stress σ in the coating because intrinsic stresses vary with deposition parameters, coating age, storage environment, and other factors. Based on measurements of similar coatings [22–24], the residual stress was expected to be tensile and in the range of $\sigma = 0$ to 150 MPa. We have not considered compressive coatings (typical of energetic-deposition methods). The pressure developed in the blister p_c was also unknown, but we estimated that the upper limit on p_c (for the case of the irreversible decomposition reaction $2H_2O_2 \rightarrow 2H_2O + O_2$ going to completion in a closed volume) is 254 MPa for a reaction temperature of 60°C, assuming ideal gas behavior for the evolved oxygen gas and incompressibility for water and peroxide; therefore, we consider blister pressures in the range of $p_c = 3$ to 200 MPa.

Figure 10 shows blister deformations resulting from several values of internal pressure p_c. The solid curves show the deformations for an intrinsic stress level of 150 MPa, while the dashed curves show the zero-intrinsic stress case [that is, the simple solution in Eq. (7)] The inset plot shows the 3-MPa case, which is difficult to resolve in the larger plot, with the axis limits reset to fit the data. Blister pressure had a profound effect on the magnitude of deformations. Blister pressures in the range of 3–200 MPa resulted in maximum blister displacements differing by two orders of magnitude: 6 nm maximum displacement for $p_c = 3$ MPa and 400 nm for $p_c = 200$ MPa. In contrast, the effect of residual stress was small, with the difference in displacements for the $\sigma = 0$ and the $\sigma = 150$ MPa cases never more than 4%. This is not surprising given that the stress parameter is $S = 0.26$ for the $\sigma = 150$ MPa

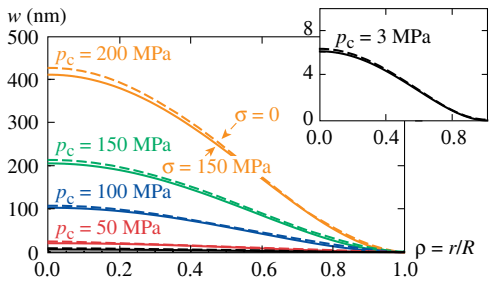

Fig. 10. Dependence of blister deformations on internal blister pressure for intrinsic coating stresses of zero (dashed curves) and 150 MPa (solid curves). Inset plot shows a larger view of the $p_c = 3$ MPa curves.

case, i.e., small. Note from Eq. (7) that the blister deformation is linear in the pressure p_c.

C. Prediction of Crack Path in Multilayer Coating and Length-Scale Considerations

In the previous section, we considered a preexisting circular debond (interface crack)—that is, we assumed that the MLD coating was not adhered to the substrate at the blister site, and the coating was free to deflect in response to pressure. To explain the characteristic fracture pattern, the interfacial crack must propagate in response to the pressure loading. If energetically favorable, it is possible for the crack to propagate at first along the interface, growing the blister to a larger diameter, but eventually the interface crack must propagate to the surface by kinking upward into the multilayer.

For an interface crack between two dissimilar materials, the ratio of the energy release rates for the kinked crack, $\mathcal{G}$, and the crack advancing in the interface, $\mathcal{G}_0$, is given by [30]

$$\frac{\mathcal{G}}{\mathcal{G}_0} = \frac{|c|^2 + |d|^2 + 2\,\mathrm{Re}[cd\,\exp(2i\bar{\psi})]}{q^2},$$
$$q = \sqrt{\frac{1-\beta^2}{1+\alpha^2}}, \qquad \bar{\psi} = \psi + \varepsilon\,\ln(a/h), \tag{8}$$

where $\mathrm{Re}(x)$ gives the real part of x. The mode mixity angle $\psi = \tan^{-1}(K_1/K_2)$ describes the crack loading, where K_1 and K_2 are the mode-1 (opening) and mode-2 (shearing) stress-intensity factors, respectively. The corrected $\bar{\psi}$ includes a term that depends on the problem length scale a/h and the bimaterial constant ε. The quantities c, d, and q are dimensionless quantities that depend on the material combination and crack kink angle. The Dundurs material moduli parameters α and β and bimaterial constant ε are defined by [31,32]

$$\alpha = \frac{\mu_1(1-\nu_2) - \mu_2(1-\nu_1)}{\mu_1(1-\nu_2) + \mu_2(1-\nu_1)},$$
$$\beta = \frac{1}{2}\left[\frac{\mu_1(1-2\nu_2) - \mu_2(1-2\nu_1)}{\mu_1(1-\nu_2) + \mu_2(1-\nu_1)}\right],$$
$$\varepsilon = \frac{1}{2\pi}\,\ln\left(\frac{1-\beta}{1+\beta}\right). \tag{9}$$

where μ_1, ν_1, and μ_2, ν_2 are the shear moduli and Poisson ratios of materials 1 and 2, respectively. Note that the material mismatch parameters α, β, and ε vanish in the homogeneous case (material 1 = material 2). We take material 1 to be the substrate and material 2 to be the coating, such that the interface crack either continues along the material 1/material 2 interface or kinks upward into material 2 with crack length a at kink angle ω, as illustrated in Fig. 11. If the interface crack is located between MLD layers rather than between the substrate and the coating, the layers beneath the crack are grouped with the substrate as a single material, and the partial multilayer above the crack is treated as material 2. Mismatch parameters α, β, and ε for relevant material combinations are shown in Table 3.

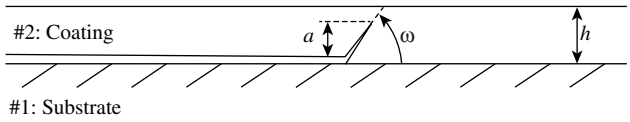

Fig. 11. Geometry of kinked crack.

The ratio of the energy release rates for the kinked crack and crack advancing in the interface $\mathcal{G}/\mathcal{G}_0$ is plotted versus kink angle for several values of $\bar{\psi}$ in Fig. 12 for the case of a BK7 substrate with a hafnia/silica MLD coating. Parameters c and d were estimated from the tabulated numerical data of He and Hutchinson [33] using linear interpolation. Note that, excepting the case of $\bar{\psi} = 0$ (corresponding to a pure mode-1 crack), a local maximum of $\mathcal{G}/\mathcal{G}_0$ exists for a nonzero value of ω, interpreted as an energetically preferred kink angle. The preferred kink angle ω_p increases with increasingly negative $\bar{\psi}$, corresponding to a greater mode-2 loading contribution. The specific value of ω_p can be determined if $\bar{\psi}$ is known.

For the case of a pressure-loaded blister with small p_c, the uncorrected mode mixity angle ψ can be expressed as the solution to $\tan(\psi) = -\cot(\gamma)$, where $\gamma = \gamma(\alpha, \beta, \eta)$ is a function of the Dundurs parameters and a geometrical parameter $\eta = h/H$ [32]. When the substrate thickness H is much larger than the coating thickness h (as in the case of an MLD thin-film coating on a thick glass substrate), $\eta \approx 0$ and $\gamma(\alpha, \beta, 0)$ can be drawn from the tabulated numerical data of Suo and Hutchinson [34] to calculate ψ. Small p_c is considered a good assumption when $p_c \ll p_0$, where p_0 is given by [32]

Table 3. Values for the Dundurs Parameters α, β, and Bimaterial Modulus ε

Material 1	Material 2	α	β	ε
BK7	MLD coating	−0.13	−0.04	0.01
BK7	HfO_2	−0.23	−0.09	0.03
HfO_2	SiO_2	0.17	0.10	−0.03
SiO_2	HfO_2	−0.17	−0.10	0.03

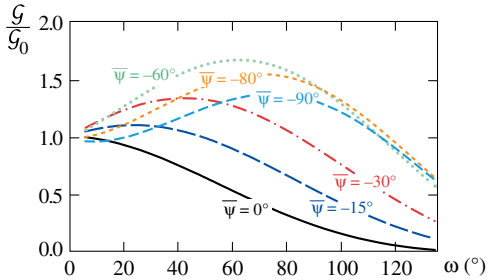

Fig. 12. Relationship between energy-release rate ratio $\mathcal{G}/\mathcal{G}_0$ and kink angle for several mode mixity angles for the BK7/MLD coating material combination.

$$p_0 = \frac{16E}{3(1-\nu^2)}\left(\frac{h}{R}\right)^4. \quad (10)$$

For the 40 μm diameter blister considered here, $p_0 = 7.4$ GPa, and the assumption is quite reasonable for a blister pressure of a few megapascals.

Determination of the corrected mode mixity $\overline{\psi}$ requires knowledge of the relevant length scale at which fracture occurs. To analyze the effect of fracture length scale, we write $\psi_B = \psi_A + \varepsilon \ln(\ell_B/\ell_A)$, where the mode mixity ψ_A is associated with fracture at the length scale ℓ_A, and ψ_B with fracture at the length scale ℓ_B. Notice that, since the bimaterial parameter ε is small, this effect will be rather small.

We assume that the mode mixity ψ_A is associated with the length scale ℓ_A comparable to the MLD coating thickness of $h = 5$ μm, and we consider two extreme cases for the effects of the length scale ℓ_B. When fracture processes occur at the length scale ℓ_B comparable to the MLD thickness (i.e., $\ell_B = \ell_A$), the correction term $\varepsilon \ln(\ell_B/\ell_A)$ vanishes, and we use the BK7/MLD mismatch parameters from Table 3 to find that $\bar{\psi} = -37.4°$. On the other hand, when fracture processes are at the length scale ℓ_B comparable to the first layer thickness ($t_1 = 131$ nm), we select the BK7/hafnia mismatch parameters because the first layer of the MLD coating adjacent to the BK7 substrate is HfO_2. In this case, $\psi_A = -35.9°$ and $\varepsilon \ln(\ell_B/\ell_A) = -5.8°$, yielding a corrected mode mixity of $\overline{\psi} = -41.7°$. The $\mathcal{G}/\mathcal{G}_0$ curves for these two extreme cases are plotted in Fig. 13. Both cases have a broad maximum in the range of $\omega_p = 45°$ to 60°.

The cross-sectional view of the FIB-bisected defect described in Section 3.A (Fig. 2) provides geometrical information about the crack propagation path in a delamination defect. The crack kinked sharply upward at the first hafnia layer (light band), and whenever it reached an interface with a new hafnia/silica layer pair. Within the silica layers (dark bands), the crack curved to a shallower angle, advancing along a trajectory nearly parallel to the layers as it approached the next hafnia layer. Measured from the bottom of each hafnia layer as shown in Fig. 2(b), the crack kink angles for the 12 layer pairs were, from the uppermost layer pair down: 65°, 63°, 58°, 56°, 66°, 66°, 55°, 52°, 55°, 55°, 66°, and 57°. These kink angles, all falling in the range of $\omega = 52°$ to 66°, are comparable to the preferred angle range of $\omega_p = 45°$ to 60° calculated in the fracture mechanics analysis, especially considering that measurements could be overestimated if the defect were not perfectly bisected during FIB milling.

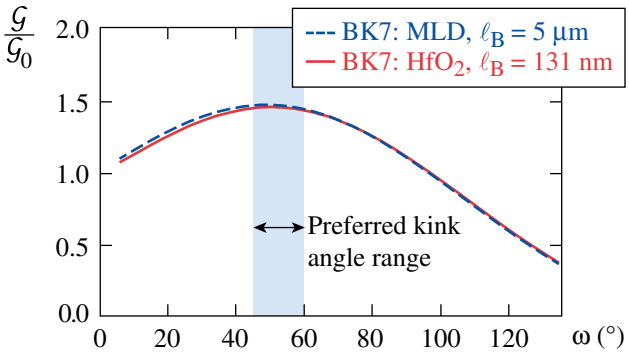

Fig. 13. Energy-release-rate ratio versus kink angle for two problem length scales: fracture involving the full MLD coating and fracture involving only the first MLD layer. The blue band shows the broad range of energetically preferred kink angles between $\omega = 45°$ and 60°.

Within the multilayer, the jagged crack trajectory can be explained by the relative stiffness of the layers in the MLD coating. When a crack propagating in a stiffer layer approaches an interface with a more-compliant layer, the crack tends to veer toward the interface, shortening its path through the stiff material. When a crack approaches an interface with a stiffer material, the crack veers away from the interface, assuming an increasingly horizontal trajectory through the compliant layer, as the energy release rate approaches zero near the interface with the stiffer material [35]. Hafnia is significantly stiffer than silica, so the fracture pattern in the defect is consistent with this behavior.

In our fracture mechanics model, we have used the literature on the interfacial or kinking cracks in a single layer bonded to a substrate. Although this analysis gives a fair representation of the kink angle, it does not take into account the full presence of the multilayer in the crack kinking mechanism: the multilayer is viewed as an equivalent single-layer coating with isotropic elastic properties. Of course, the actual multilayer is anisotropic, with different elastic properties parallel to and normal to the interface with the substrate. A full fracture mechanics analysis would include the presence of the individual single layers and, given the pressure in the interfacial crack, determine the traction variation with distance away from the crack tip, and therefore find the mode mixity directly. We are initiating this work.

6. Conclusions

A mechanism has been proposed for the formation of peroxide-induced delamination defects in multilayer coatings. The mechanism, involving pressure development in a small cavity in the coating, is supported by experimental results and microscopic observation of defects. A fracture mechanics model was developed to explain the deformation and failure of the MLD. The characteristic fracture pattern of the defect was found to be consistent with the crack path that maximizes energy release rate.

The authors thank Dr. James Oliver for helpful discussions. Two of the authors (H. P. H. L. and K. M.) acknowledge support through Horton Fellowships at the Laboratory for Laser Energetics. This material is based upon work supported by the U.S. Department of Energy under Award DE-EE0006033.000 and by the Department of Energy National Nuclear Security Administration under Award DE-NA0001944.

References and Note

1. M. Alvisi, M. Di Giulio, S. G. Marrone, M. R. Perrone, M. L. Protopapa, A. Valentini, and L. Vasanelli, "HfO_2 films with high laser damage threshold," Thin Solid Films **358**, 250–258 (2000).
2. X. Cheng, Z. Shen, H. Jiao, J. Zhang, B. Ma, T. Ding, J. Lu, X. Wang, and Z. Wang, "Laser damage study of nodules in electron-beam-evaporated HfO_2/SiO_2 high reflectors," Appl. Opt. **50**, C357–C363 (2011).
3. J. Neauport, E. Lavastre, G. Razé, G. Dupuy, N. Bonod, M. Balas, G. de Villele, J. Flamand, S. Kaladgew, and F. Desserouer, "Effect of electric field on laser induced damage threshold of multilayer dielectric gratings," Opt. Express **15**, 12508–12522 (2007).
4. Y. G. Shan, H. B. He, Y. Wang, X. Li, D. W. Li, and Y. A. Zhao, "Electrical field enhancement and laser damage growth in high-reflective coatings at 1064 nm," Opt. Commun. **284**, 625–629 (2011).
5. Y. Shan, H. He, C. Wei, S. Li, M. Zhou, D. Li, and Y. Zhao, "Geometrical characteristics and damage morphology of nodules grown from artificial seeds in multilayer coating," Appl. Opt. **49**, 4290–4295 (2010).
6. J. F. DeFord and M. R. Kozlowski, "Modeling of electric-field enhancement at nodular defects in dielectric mirror coatings," Proc. SPIE **1848**, 455–472 (1993).
7. M. D. Feit, L. W. Hrubesh, A. M. Rubenchik, and J. N. Wong, "Scaling relations for laser damage initiation craters," Proc. SPIE **4347**, 316–323 (2001).
8. W. Kong, S. Liu, J. Shen, Z. Shen, J. Shao, Z. Fan, and J. Yao, "Study on LIDT of MDGs for different fabrication processes," Microelectron. Eng. **83**, 1426–1429 (2006).
9. H. P. Howard, A. F. Aiello, J. G. Dressler, N. R. Edwards, T. J. Kessler, A. A. Kozlov, I. R. T. Manwaring, K. L. Marshall, J. B. Oliver, S. Papernov, A. L. Rigatti, A. N. Roux, A. W. Schmid, N. P. Slaney, C. C. Smith, B. N. Taylor, and S. D. Jacobs, "Improving the performance of high-laser-damage-threshold, multilayer dielectric pulse-compression gratings through low-temperature chemical cleaning," Appl. Opt. **52**, 1682–1692 (2013).
10. K. L. Marshall, Z. Culakova, B. Ashe, C. Giacofei, A. L. Rigatti, T. J. Kessler, A. W. Schmid, J. B. Oliver, and A. Kozlov, "Vapor-phase-deposited organosilane coatings as 'hardening' agents for high-peak-power laser optics," Proc. SPIE **6674**, 667407 (2007).
11. H. A. Macleod and D. Richmond, "Moisture penetration patterns in thin films," Thin Solid Films **37**, 163–169 (1976).
12. H. K. Pulker, "Characterization of optical thin films," Appl. Opt. **18**, 1969–1977 (1979).
13. H. Howard, J. C. Lambropoulos, and S. Jacobs, "Dependence of thermal stresses on substrate thickness during wet processing of large coated optics," in *Optical Fabrication and Testing*, OSA Technical Digest (online) (Optical Society of America, 2012), paper OW3D.3.
14. B. Ashe, K. L. Marshall, C. Giacofei, A. L. Rigatti, T. J. Kessler, A. W. Schmid, J. B. Oliver, J. Keck, and A. Kozlov, "Evaluation of cleaning methods for multilayer diffraction gratings," Proc. SPIE **6403**, 64030O (2007).
15. B. Ashe, C. Giacofei, G. Myhre, and A. W. Schmid, "Optimizing a cleaning process for multilayer-dielectric-(MLD) diffraction grating," Proc. SPIE **6720**, 67200N (2007).
16. S. Chen, B. Sheng, X. Xu, and S. Fu, "Wet-cleaning of contaminants on the surface of multilayer dielectric pulse compressor gratings by the piranha solution," Proc. SPIE **7655**, 765522 (2010).
17. H. M. Jensen, "Analysis of mode mixity in blister tests," Int. J. Fract. **94**, 79–88 (1998).
18. J. B. Oliver, T. J. Kessler, H. Huang, J. Keck, A. L. Rigatti, A. W. Schmid, A. Kozlov, and T. Z. Kosc, "Thin-film design for multilayer diffraction gratings," Proc. SPIE **5991**, 59911A (2005).
19. MLD coating samples were dried with a filtered nitrogen gun because this standard technique avoids water spots and particle accumulation on the optic's surface. Delicate, etched MLD grating samples would not be dried with nitrogen, however, because of the potential for pillar damage. Nitrogen drying is not expected to play a role in the defect formation mechanism; defect formation results were found to be similar on ambient-dried MLD grating samples and nitrogen-dried MLD coating samples.
20. K. Mehrotra, H. P. Howard, S. D. Jacobs, and J. C. Lambropoulos, "Mechanical characterization of 'blister' defects on optical oxide multilayers using nanoindentation," in *Nanocomposites, Nanostructures and Heterostructures of Correlated Oxide Systems*, T. Endo, H. Nishikawa, N. Iwata, A. Bhattacharya, and L. W. Martin, eds., Mat. Res. Soc. Symp. Proc. (Cambridge University, 2012), Vol. **1454**, pp. 215–220.
21. H. Leplan, B. Geenen, J. Y. Robic, and Y. Pauleau, "Residual stresses in evaporated silicon dioxide thin films: correlation with deposition parameters and aging behavior," J. Appl. Phys. **78**, 962–968 (1995).
22. J. B. Oliver, P. Kupinski, A. L. Rigatti, A. W. Schmid, J. C. Lambropoulos, S. Papernov, A. Kozlov, C. Smith, and R. D. Hand, "Stress compensation in hafnia/silica optical coatings by inclusion of alumina layers," Opt. Express **20**, 16596–16610 (2012).
23. J. F. Anzellotti, D. J. Smith, R. J. Sczupak, and Z. R. Chrzan, "Stress and environmental shift characteristics of HfO_2/SiO_2 multilayer coatings," Proc. SPIE **2966**, 258–264 (1997).
24. J. B. Oliver, P. Kupinski, A. L. Rigatti, A. W. Schmid, J. C. Lambropoulos, S. Papernov, A. Kozlov, and R. D. Hand, "Modification of stresses in evaporated hafnia coatings for use in vacuum," in *Optical Interference Coatings*, OSA Technical Digest (Optical Society of America, 2010), paper WD6.
25. R. Thielsch, A. Gatto, and N. Kaiser, "Mechanical stress and thermal-elastic properties of oxide coatings for use in the deep-ultraviolet spectral region," Appl. Opt. **41**, 3211–3217 (2002).
26. R. Thielsch, A. Gatto, J. Heber, and N. Kaiser, "A comparative study of the UV optical and structural properties of SiO_2, Al_2O_3, and HfO_2 single layers deposited by reactive evaporation, ion-assisted deposition and plasma ion-assisted deposition," Thin Solid Films **410**, 86–93 (2002).
27. S. L. Dole, O. Hunter, and C. J. Wooge, "Elastic properties of monoclinic hafnium oxide at room temperature," J. Am. Ceram. Soc. **60**, 488–490 (1977).
28. M. J. Bamber, K. E. Cooke, A. B. Mann, and B. Derby, "Accurate determination of Young's modulus and Poisson's ratio of thin films by a combination of acoustic microscopy and nanoindentation," Thin Solid Films **398–399**, 299–305 (2001).
29. Optical Glass Data Sheets, available online at http://www.schott.com/advanced_optics/us/abbe_datasheets/schott_datasheet_all_us.pdf, Schott, North America.
30. M.-Y. He and J. W. Hutchinson, "Kinking of a crack out of an interface," J. Appl. Mech. **56**, 270–278 (1989).
31. J. Dundurs, "Discussion: 'edge-bonded dissimilar orthogonal elastic wedges under normal and shear loading' (Bogy, D. B., 1968, ASME J. Appl. Mech., 35, pp. 460–466)," J. Appl. Mech. **36**, 650–652 (1969).
32. J. W. Hutchinson and Z. Suo, "Mixed mode cracking in layered materials," in *Advances in Applied Mechanics*, J. W. Hutchinson and T. Y. Wu, eds. (Academic, 1992), Vol. **29**, pp. 163–191.
33. M.-Y. He and J. W. Hutchinson, "Kinking of a crack out of an interface: tabulated solution coefficients," Tech. Rep. MECH-113A (Harvard University, Division of Applied Sciences, 1989).
34. Z. Suo and J. W. Hutchinson, "Interface crack between two elastic layers," Int. J. Fract. **43**, 1–18 (1990).
35. M.-Y. He and J. W. Hutchinson, "Crack deflection at an interface between dissimilar elastic materials," Int. J. Solids Struct. **25**, 1053–1067 (1989).